



ELSEVIER

Available online at www.sciencedirect.com

SCIENCE @ DIRECT®

Earth and Planetary Science Letters 217 (2004) 409–424

EPSL

www.elsevier.com/locate/epsl

Using stress deflections to identify slip events in fault systems

Catherine Homberg*, Jacques Angelier, Françoise Bergerat, Olivier Lacombe

Laboratoire de Tectonique, University P. and M. Curie, UMR 7072-CNRS, Case 129, 4 place Jussieu, 75252 Paris Cedex 05, France

Received 24 February 2003; received in revised form 10 October 2003; accepted 11 October 2003

Abstract

A new approach for identifying past slip events in strike-slip fault systems without geological markers is presented. A 2-D distinct element modeling code is used to simulate the stress distribution around a strike-slip fault zone after a major slip event. Mature and immature fault zones are investigated. Slip on the fault is responsible for stress rotations near the active fault strand. Series of experiments reveal that the stress deflections are qualitatively the same whatever the fault strike, fault friction, and far-field differential stresses. For a left-lateral fault, stresses are rotated clockwise in the two compressive quadrants near the fault tips and counterclockwise in the two extensive quadrants. The stress field signature of a slip event thus highlights the extent of the active fault strand. Conversely, the reconstruction of paleostress fields through inversion of minor striated faults that commonly follow slip on the master fault and the analysis of their deflections allow recognition of the fault strands that slipped in a close or remote past. Application to the left-lateral Pontarlier Fault Zone in the Jura fold-and-thrust belt (France), Late Cenozoic in age, shows that the fault activity has migrated northward, in agreement with the in-sequence development of the mountain belt.

© 2003 Elsevier B.V. All rights reserved.

1. Introduction

Fault activity involves composite deformation mechanisms at various time scales. Earthquakes producing instantaneous ruptures and steady-state slip may occur. Instrumental seismology reveals that earthquakes are variable in size and no simple relation accounts for their succession in space and time. Even when considering a long time scale, the activity of individual faults is also irregular as suggested by the variability of fault-slip rates (e.g. [1]). Our understanding of

the short-term behavior of faults has benefited from the increasing mass of seismological data on the present-day activity of faults. Universal characteristics have emerged from various catalogs, like the Gutenberg–Richter power law. However, how fault activity migrates through time along a fault zone remains poorly understood. As an example, earthquakes may follow either the Gutenberg–Richter model (e.g. [2,3]), implying that events of all sizes occur between the largest expected events on a fault, or may follow the characteristic model (e.g. [4,5]), implying that each fault is subject to events of the same order of magnitude separated by quiescent periods. As emphasized by Kagan [6], the limitation in size of the available data sets precludes any choice between these two models.

To understand the faulting process, the long-

* Corresponding author. Tel.: +33-1-44-27-52-74;
Fax: +33-1-44-27-50-85.

E-mail address: catherine.homberg@lgs.jussieu.fr
(C. Homberg).

term behavior of faults cannot be ignored because the whole fault activity cannot be extrapolated from their seismic behavior. Several critical aspects of fault activity evolve through time, like the stress distribution in the crust and the fault shear strength (e.g. [7–9]). Little is known about the long-term activity of individual faults because, in many cases, geological observation does not give more than the total accumulated slip. Deciphering the migration of active fault strands through millions of years would require proper markers of various ages, which in most cases are absent. When folding or tilting are genetically related to fault slip, unconformities may be used to identify the periods of activity along the fault zone, but in practice this kind of information is too incomplete to allow reconstruction of the migration of active fault strands through time.

In this paper, we present a new method that may help to identify past slip events along fault systems. In the first section, we show that the static stress pattern that follows slip on a fault strand exhibits characteristic stress deflections that define a stress field signature, hereafter called SFS. We then describe how the paleostress fields in fault systems can be reconstructed and compared with the SFS of a slip event to identify the fault strand active in the past. The method is thought to apply whatever the age of faulting, so that both active and ancient fault systems can be investigated. A regional application to a Tertiary fault in the Jura mountain belt, eastern France, is presented in the second section.

2. Paleostress analysis as a key to identify past slip events in fault zones

In order to investigate the past activity of fault systems, we have developed a method for identifying ancient active fault strands. Various mechanical approaches, such as dislocation model [10] or crack theory [11], concur that slip on a fault induces significant changes of the static stress field (in both magnitude and direction) in the surrounding rock volume. This process has been validated by successful applications of the stress triggering theory to various faults (e.g.

[7,12]), according to which most aftershocks occur where the Coulomb stress has increased after the main rupture. Similarly, paleostresses in ancient deformed domains and recent stresses in active zones reconstructed by inversion of fault-slip data exhibit rotations near faults (e.g. [13–15]). This suggests that the past activity of faults was similarly associated with significant changes in the near stress field. We show here that conversely the reconstruction of the paleostress fields and the analysis of their deflections near faults allow recognition of the strands that have slipped in the past.

2.1. Modeling a slip event in a fault zone

Because at this stage the aim is not to predict which part of the fault system fails, but to describe the static stress field that follows slip on a fault, we simply consider the fault segment where slip takes place. The active segment is idealized as

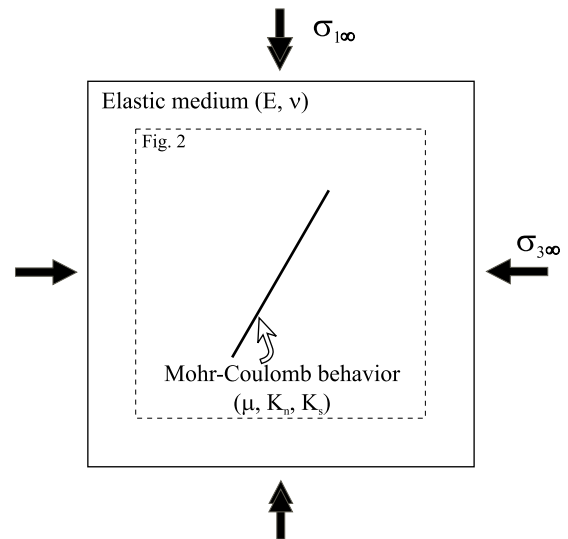


Fig. 1. 2-D mechanical model of a strike-slip event (horizontal view). The active fault (thick line) is idealized as a slipping line in an elastic medium. μ , K_n and K_s : coefficient of friction, normal and shear stiffness of the fault. E and ν : Young's modulus and Poisson's ratio of the elastic medium. The imposed biaxial loading corresponds to the minimum and maximum far-field horizontal principal stresses $\sigma_{1\infty}$ (double arrows) and $\sigma_{3\infty}$ (single arrows). See text for further explanation.

a planar discontinuity in an elastic medium (Fig. 1). The slipping surface may be more complex, involving several faults and curved segments. Such geometrical complexities are crucial in rupture nucleation (e.g. [16]). As we do not address nucleation–propagation processes, a planar geometry of the slipping zone is a reasonable first approximation for characterizing the static stress field that follows a slip event. Geometrical irregularities are considered in the second section through a case example where we show that they do not significantly alter the conclusions inferred from our simplified model.

Various modeling approaches offer the possibility to calculate the changes in the static stresses induced by slip on a fault. In seismotectonic studies, the static stress changes are often considered through dislocation models in order to estimate how the main shock guides distribution and timing of the subsequent deformation [7]. Such models usually consider a discontinuity subjected to a given slip in an elastic half-space and without external loading. They thus deliberately neglect the tectonic loading to determine the contribution of the sole main rupture (Coulomb stress change) to the stress field. In this work, we used a 2-D distinct element technique [17]. This mechanical approach considers the total stress field, including the contribution of the slipping fault as well as the contribution of the far-field loading; the results may thus be directly compared to the stress field reconstructed with fault-slip data. In this paper, we address the case of vertical strike-slip faults. Because most of the deformation occurs in the horizontal plane, it can be analyzed through a 2-D approach.

The resulting static stress field that follows slip of a strike-slip fault is discussed in the light of a

previous 2-D modeling work [14]. The stress field was computed here in the horizontal plane for a left-lateral strike-slip fault in an elastic medium (Fig. 1), subjected to a biaxial loading simulating the far-field horizontal maximum and minimum principal stresses, $\sigma_{1\infty}$ and $\sigma_{3\infty}$ (compression is positive). The fault obeys a Mohr–Coulomb behavior. According to experiments of Byerlee [18], the failure conditions under moderate crustal stresses are independent of the rock cohesion. Slip occurs when the shear stress τ acting on the fault plane reaches a critical level, τ_c , written as follows:

$$\tau_c = \mu \sigma_n$$

where μ is the fault coefficient of friction and σ_n is the normal stress acting on the fault plane. Slip on the fault follows a linear normal and shear behavior described as:

$$\tau = K_s U_s$$

and

$$\sigma_n = K_n U_n$$

where K_s and K_n are the shear and normal stiffness of the fault, U_s and U_n are the shear and normal displacement on the fault plane, and τ and σ_n are the shear and normal stress acting on the fault plane. The elastic parameters of the medium, the fault properties, and far-field stresses considered here are listed in Table 1.

Assuming that the planar geometry of the active fault strand is a reasonable first approximation, the slipping discontinuity considered in our model may be regarded as a fault or a fault segment that slips. This model (Fig. 1) thus allows us to describe the static stress state near a strike-slip fault system after part of it has slipped.

Table 1
Model parameters

Elastic modulus (host-Fault parameters ing rock)						Tectonic loading		Elastic modulus (fault body)
E	ν	θ	μ	K_n	K_s	$\sigma_{1\infty}$	$\sigma_{3\infty}$	E'
60 GPa	0.25	0–90°	0.01–1	200 GPa	200 GPa	20–100 MPa	10 MPa	6–30 GPa

E and ν : Young's modulus and Poisson ratio of the hosting rock; θ : angle of the fault relative to $\sigma_{1\infty}$; μ , K_n and K_s : coefficient of friction, normal and shear stiffness of the fault; E' : Young's modulus of the weak fault zone body (see Fig. 4); $\sigma_{1\infty}$ and $\sigma_{3\infty}$: maximum and minimum principal far-field stresses (compression positive).

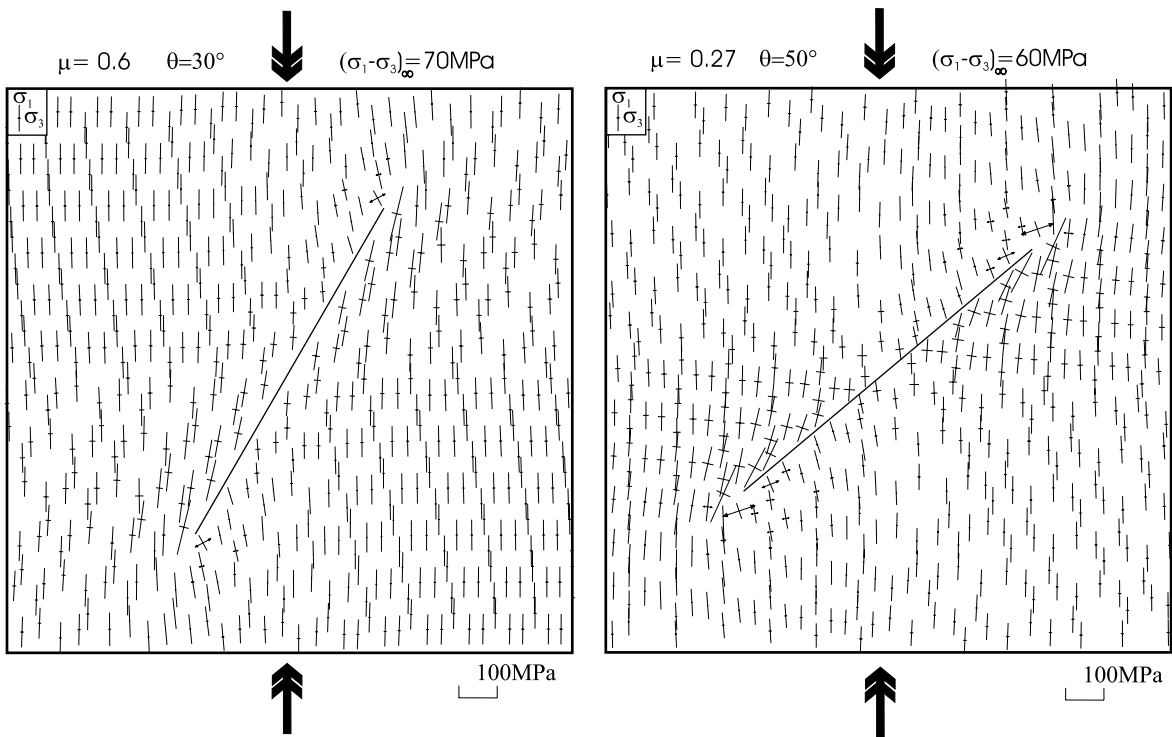


Fig. 2. Static stress distribution following a strike-slip event. 2-D distinct element modeling (DEM). The angle, θ , of the fault relative to $\sigma_{1\infty}$, the coefficient of friction, μ , of the fault (thick line), and the far-field differential stress, $(\sigma_1 - \sigma_3)_\infty$, are indicated for the two ruptures cases (a) and (b). Double arrows: direction of $\sigma_{1\infty}$. Magnitude of σ_1 and σ_3 are proportional to the line length (see scale). See Fig. 1 for input of the model. Stress marks are plotted with the deformed grid of the distinct elements.

2.2. Static stress field following a strike-slip event

Fig. 2 shows the static stress field following slip of two cases of fault segment. In Fig. 2a, slip takes place on a fault with a coefficient of friction of 0.6 and oriented at an angle of 30° to the far-field maximum stress, $\sigma_{1\infty}$, for a far-field differential stress $(\sigma_1 - \sigma_3)_\infty$ of 70 MPa. In Fig. 2b, slip occurs on a fault with a coefficient of friction of 0.27 and oriented at 50° to σ_1 , for a far-field differential stress $(\sigma_1 - \sigma_3)_\infty$ of 60 MPa. In both cases, slip induces changes in the near-field static stress orientation, resulting in a heterogeneous stress distribution around the fault. The stress distribution has been computed, as in Fig. 2, for various fault strikes relative to the far-field stresses (from faults parallel to $\sigma_{1\infty}$ to faults perpendicular to $\sigma_{1\infty}$), for a large range of fault properties (μ ranging from 0.01 to 1), and for various far-field differential stresses ($\sigma_{1\infty} - \sigma_{3\infty}$ ranging from

10 MPa to 100 MPa) (see Table 1). These multiple experiments have shown that regardless of the values of the parameters within reasonable bounds, the changes in the stress orientation near the active fault strand are qualitatively the same. The stress distribution has the following characteristics (Fig. 3). First, stress deviations occur near the slipping fault (at a distance that does not exceed half the fault length); far away from the fault, the stress field is homogeneous and similar to the far-field stresses. Second, stress deviations are maximum near fault tips. Third, the stress distribution is symmetrical relative to the fault center; for a left-lateral fault, and looking from the fault center towards a fault tip, the stresses are rotated clockwise by β degrees in the area right of the fault tip (compression quadrant) and counterclockwise by α degrees in the area left of the fault tip (extension quadrant) (Fig. 3). For a right-lateral fault, the pattern is the mirror im-

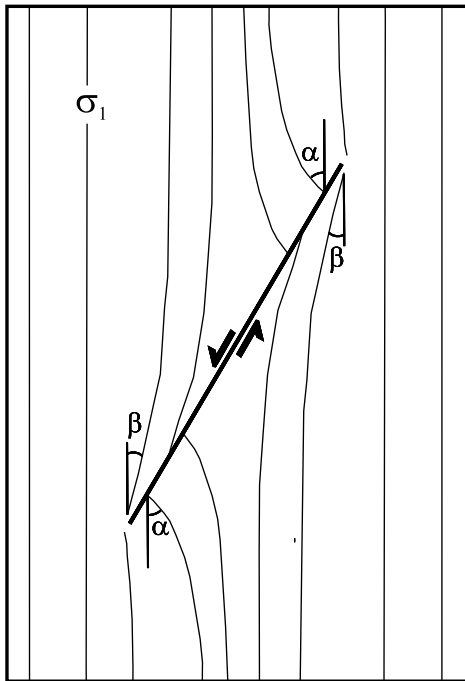


Fig. 3. SFS of a strike-slip event. α and β : maximum amount of counterclockwise and clockwise stress rotations relative to the far-field directions. The stress field following the slip event (thin line and double arrows) exhibits characteristic stress deflections near the compressive and extensive quadrants close to the fault tips.

age of that shown in Fig. 3. Changing the parameters of the model results in variations of the amount of stress rotation, but does not modify the sense and the location where these rotations occur.

In the light of these results, it follows that the distribution of the static stresses around an active fault strand shows a typical pattern (Fig. 3) which remains qualitatively the same whatever the strike and coefficient of friction of the fault and whatever the magnitudes of the far-field principal stresses. Reciprocally, even if individual faults constituting the fault system may have various trends and shear strengths, faults or fault segments that have been activated at any time in the loading history can be identified if the corresponding static stress field is known (large variations of friction along faults being not considered herein). The method for reconstructing the static stress fields associated with the past activity of

fault zones will be considered at the end of this section.

2.3. Static stress field following strike-slip event in a mature fault zone

Major faults in fault systems, like those forming plate boundaries, exhibit a meso- and microscopic structural fabric that may modify the rheological properties of the rock inside the fault zone. Such mature fault zones exhibit an almost elliptical damage zone with crushed rocks and containing a large number of faults and fractures, whereas the host rock may be regarded as a continuous and undeformed medium. Due to this structural fabric, the host rock and the rock inside the fault zone may exhibit contrasting elastic strengths. For such well-developed or mature faults, the activity occurs in a weak body (the fault zone) imbedded in a stronger and stable volume (the host rock).

We have conducted a second set of models simulating slip along a segment of a mature fault zone (Fig. 4). As for the first models (Fig. 1), slip takes place along a planar discontinuity with a Mohr–Coulomb behavior, but the fault is

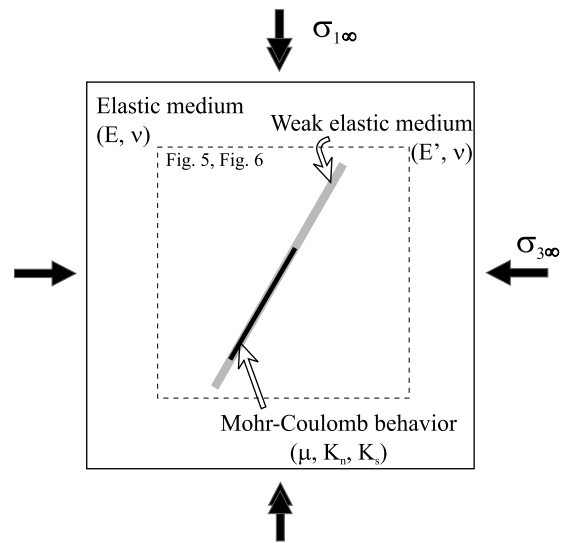


Fig. 4. 2-D mechanical model of a strike-slip event in a mature fault zone (horizontal view). The slipping fault (thick line) is imbedded in a weak fault zone body (shaded area) with a small Young's modulus, E' . Same symbols as in Fig. 1.

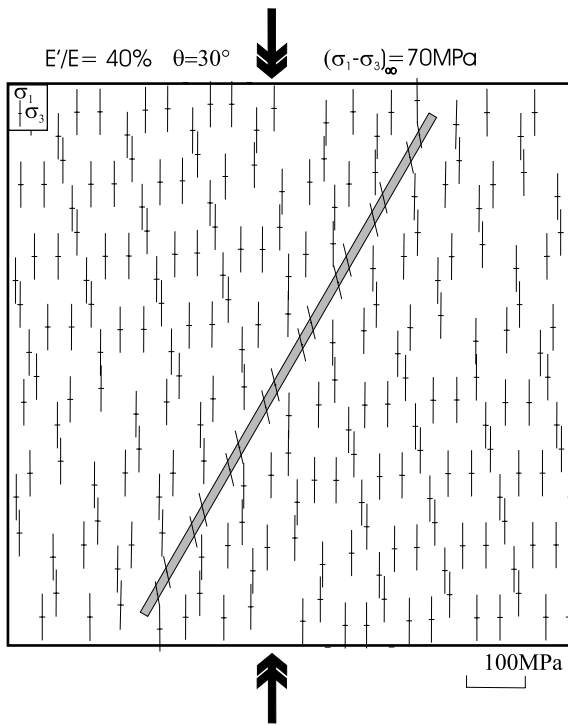


Fig. 5. Static stress distribution during quiescent periods near a mature fault zone (2-D DEM). Weak fault zone body with E' Young's modulus in gray. The view is a zoom on the fault zone (see Fig. 4). Same symbols as in Fig. 2.

now included in an elongated elastic body with a small Young's modulus that simulates the weak fault zone body. The fault zone body and the active fault strand are imbedded, as previously, in an elastic, resistant medium representing the host rock (Fig. 4). The tectonic loading, fault properties, and elastic properties of the hosting rock are the same as in the previous models (Table 1).

For clarity, we first describe the static stress field in a mature fault zone where no slip occurs. The stress field illustrated in Fig. 5 thus corresponds to the stress field during a quiescent period. It is homogeneous (and identical to the far-field stress) except inside the fault zone where stresses are rotated so that the direction of compression tends to become perpendicular to the fault zone strike. If the fault zone is extremely

weak (i.e. with a very small Young's modulus), the stress rotation inside the fault zone becomes larger. Because no slip occurs here, such stress changes are not related to the fault activity; they are permanent features that exist since faults, fractures, breccia or gouges have developed and have reduced the elastic strength of fault zone and are thus related to the structural fabric of the weak fault zone body.

Fig. 6 shows the static stress distribution associated with slip occurring along a fault strand in a mature fault zone. The imposed tectonic loading, the orientation and properties of the slipping fault are identical to those considered in Fig. 2a. The stress changes (Fig. 6) are of two types: the first type occurs inside the fault zone where the direction of compression tends to become perpendicular to the fault zone trend; this stress rotation results from the weakness of the fault zone rocks

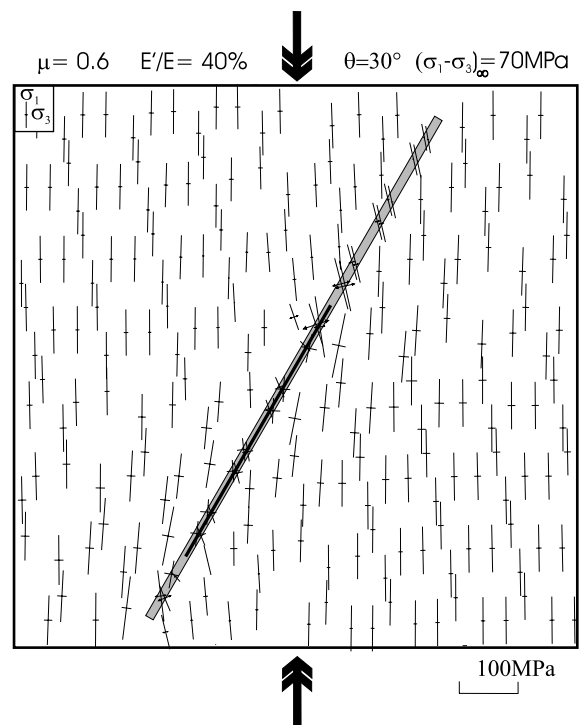


Fig. 6. Static stress distribution following a strike-slip event in a mature fault zone (2-D DEM). Weak fault zone body with E' Young's modulus in gray. Slipping portion of the fault zone shown as thick black line. The view is a zoom on the fault zone (see Fig. 4). Same symbols as in Fig. 2.

(compare Figs. 6 and 5). The second type of stress change occurs in the host rock close to the sliding fault and resembles that associated with a slip event along a moderately deformed fault zone (compare Figs. 6 and 2). These stress rotations, however, are slightly smaller. In the host rock surrounding the active fault, stresses thus change in direction because both the slipping fault and the tectonic loading contribute to the total stress field.

As for the first models, a large range of fault properties, fault orientation and tectonic loading, as well as more or less weak fault zone body (i.e. with a Young's modulus 2–10 times smaller than that of the host rock) has been investigated (Table 1). These experiments led us to define again a specific pattern of the static stress field associated with slip occurring in a mature fault zone (Fig. 7). As before, changing the parameters results in different amounts of stress rotation, but does not

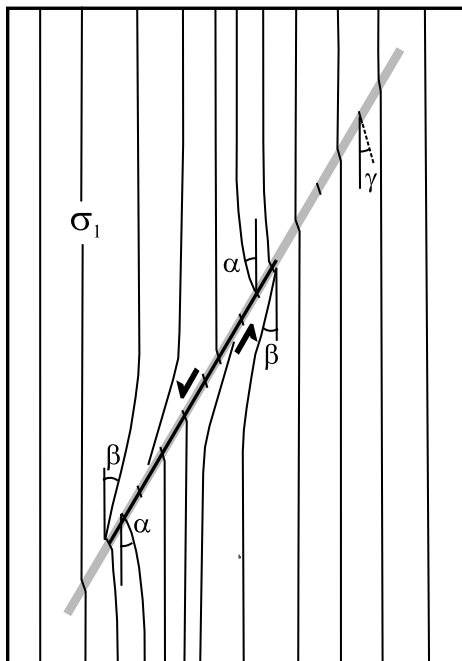


Fig. 7. SFS of a strike-slip event in a mature fault zone. α and β : maximum amount of counterclockwise and clockwise stress rotations in the host rock. γ : stress rotation amount inside the fault zone. Beside stress rotation inside the fault zone body, the stress field exhibits characteristic stress deflections in the compressive and extensive quadrants close to the tips of the active fault segment.

qualitatively change the stress distribution (stress-axes are rotated in the same sense at the same locations). Increasing the weakness of the fault zone results in an increase of the stress rotation inside the fault zone body (labeled with the angle γ), and in a slight decrease of the stress rotation in the host rock surrounding the slipping fault (labeled with the two angles α and β). Changing the orientation and friction of the fault or changing the far-field stress magnitude modifies the amount of stress rotation, α and β , in the host rock, but does not affect the amount of stress rotation, γ , inside the fault zone.

We conclude that slip along fault strands of mature and moderately deformed fault zones is followed by characteristic rotations of the near-field stresses whatever the fault strike and properties and thus has a unique SFS. The SFS consists of stress deflections close to the active fault tips, in opposite sense in the compressive and extensive quadrants. Therefore, the location and extent of ancient active fault strands may be inferred from analysis of the stress deflections near faults.

2.4. Using secondary faults to reconstruct static stress fields associated with past slip events

The past local stress states along fault zones may be inferred from analysis of fault-slip data collected in sites of measurement through inversion methods (e.g. [19]). The inversion process allows determination of the orientation of the three principal stresses, σ_1 , σ_2 and σ_3 , as well as the stress ellipsoid shape ratio (the ratio between differences of principal stress magnitudes) without any assumption about the crustal strength. The uncertainty on the orientations of the stress axes depends on the 3-D distribution of the fault-slip data. When fault-slip data display various attitudes and include conjugate sets, the accuracy on the direction and plunge of the principal axes is about 10°. Because minor faults are found in highly (e.g. [20,21]) as well as moderately deformed areas (e.g. [22]), their collection and inversion offer the possibility to reconstruct the near-field (close to faults) and far-field stresses, provided that natural or artificial outcrops exist. Fault strands that have slipped in the past will

thus be revealed by confrontation of the reconstructed paleostress field with the SFS of a slip event.

Fig. 8 illustrates a time period during which activity has migrated along the fault zone and has involved two different fault strands. Each slip episode induces deflections of the near-stress field (Fig. 8A). Because slip occurred along a different fault segment for each period, the local stress orientation changes through time, particularly close to the active fault tips (Fig. 8B). In these areas, secondary faults following each event thus display different orientations (Fig. 8C). For such a heterogeneous fault population, the inversion process fails to determine a unique stress state with acceptable misfits, thus revealing the superimposition of different stress states (Fig. 9). These stress states are computed by performing an inversion on each of the homogeneous subsets. Classification of the fault population into homogeneous subsets is guided by field observation,

like relative chronology between faults (see below) and fault misfits between actual fault slips and slips predicted by the computed tensor. Additional stress markers like stylolitic peaks, the direction of which corresponds to σ_1 , or tension gashes, the normal of which is parallel to σ_3 , may help to determine the numbers of superimposed stress states. The succession of the superimposed stress states is obtained by relative chronology data between brittle structures (e.g. cross-cutting relationships between faults, superimposition of striations on fault surfaces) or criteria establishing the age of structures relative to folding (see last section for example). In simple cases, such as for the two periods considered in Fig. 8, the compilation of the local stress state successions allows reconstruction of the successive stress fields. Each of these stress fields exhibits a SFS that highlights the occurrence and location of slips along the fault zone. The local chronologies indicate the succession of these two slip events.

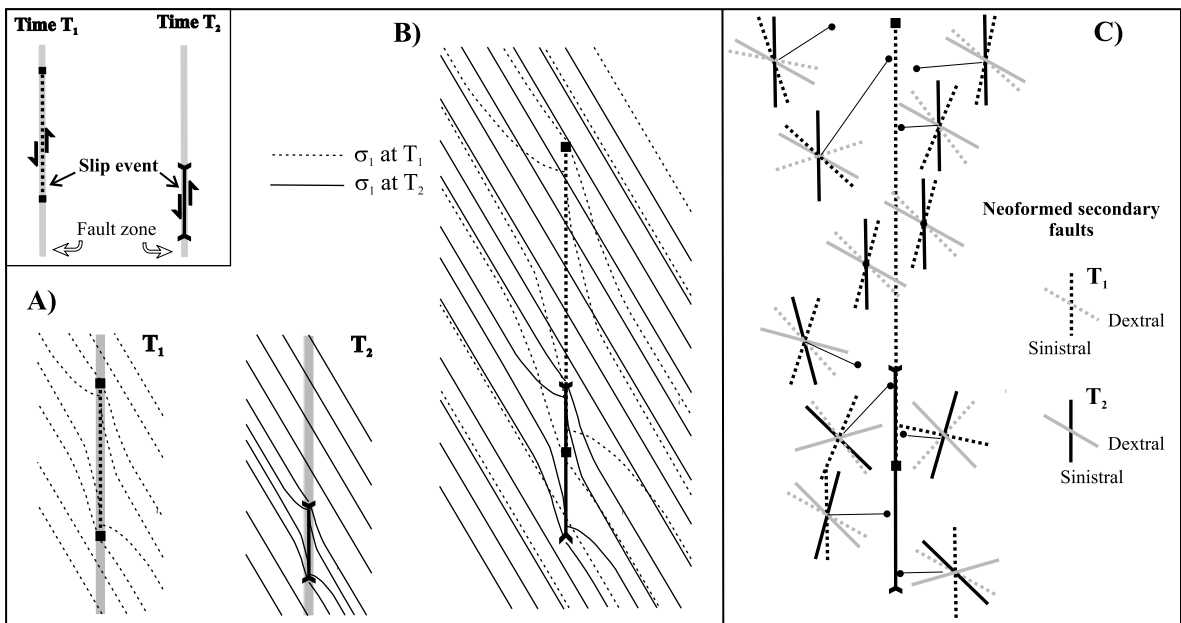


Fig. 8. Stress evolution with the migration of fault activity. The fault zone fails at times T_1 and T_2 . The stress trajectories after each slip event are shown separately (A) and superimposed (B). Secondary neofomed faults (taking an internal friction angle of 30°) following each slip event are illustrated at selected localities (C). Orientation of secondary faults at times T_1 and T_2 differs because stress direction changes after each slip event, especially near fault tips.

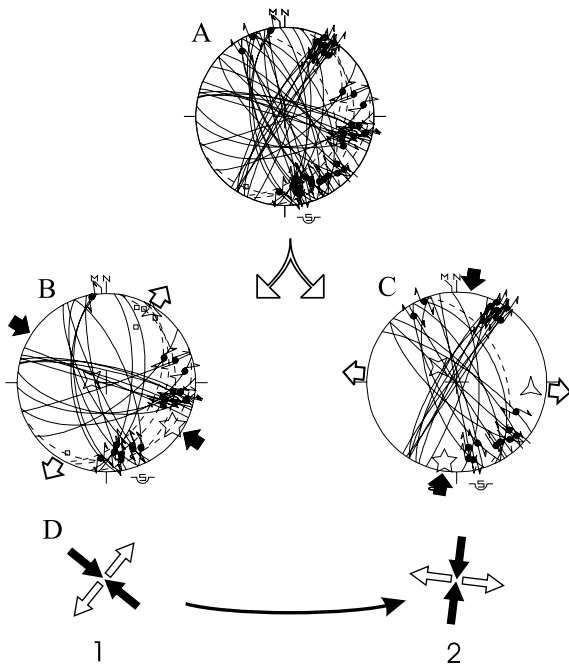


Fig. 9. Recognition of stress change through minor fault-slip data analysis. Example of a site near the Pontarlier Fault Zone. Mechanical incompatibilities between minor faults (A) collected in a natural outcrop indicate that the fault population is polyphase. Mechanical incompatibilities, misfits between the calculated and actual slips, as well poles of tension gashes, are used to divide the population into homogeneous subsets (B,C). The succession of the two stress states (D) is inferred from cross-cutting of the sinistral slips by the dextral slips on the N–S to NNW–SSE planes. Continuous lines: fault planes. Slickenside lineations for strike-slip motion in dots with double arrows. Squares: pole to tension gashes. Dashed lines: bedding planes. Gray stars with 5, 4, 3 arms: σ_1 , σ_2 , and σ_3 , respectively. Convergent black and divergent white large black arrows show directions of σ_1 and σ_3 , respectively.

3. Application to the Tertiary Pontarlier Fault Zone (Jura Mountains)

3.1. Structure and origin of the Pontarlier Fault Zone

The Pontarlier Fault Zone (PFZ) is a 70-km-long left-lateral strike-slip fault in the Jura fold-and-thrust belt (Fig. 10). It belongs to the fault system of the western Alpine orogenic belt. Left-lateral displacement occurred along the PFZ during the Jura tectogenesis that started in the Late

Miocene and ended in the Early Pliocene ([23,24] for a review). The PFZ is presently inactive, although nearby small ($M < 3$) earthquakes may indicate some present-day activity. The PFZ consists of two main, right-stepping en échelon faults, spaced 2 km apart (Fig. 10). The northern fault strikes N–S and is 50 km long. The southern one runs 20 km with a NNW–SSE trend, with a possible extension to the south. A 7-km-long fault, trending N030°, links the two master faults across the compressive step. The PFZ strike may vary slightly, but no major bend exists, except near the compressive step where the two main faults curve slightly. A few short secondary faults exist. The two longer ones are 5 km long on average and run parallel to the main faults. One of them

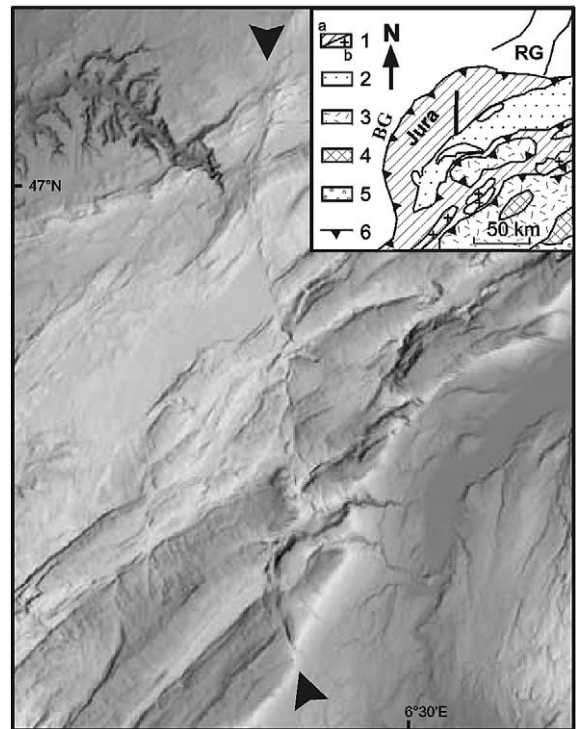


Fig. 10. Location and internal structure of the PFZ. The PFZ is marked by triangles on a DEM using the VISUAL-DEM 1995 data base. Inset shows the PFZ (thick line) in the structural frame of the Alpine domain. 1: External zones; a, cover (Jura and Helvetic nappes) and b, basement. 2: Molasse Basin. 3 and 4: Penninic units and Austro-Alpine domain (internal zones). 5: Pliocene–Quaternary infill of the Po plain. 6: Major thrusts. RG and BG: Rhine and Bresse grabens. DM provided by B. Van Vliet-Lanoë.

branches to the northern fault and the other ends within the compressive step (Fig. 11).

The fault planes of the two master faults are exposed at a few places, mostly in quarries. They are nearly vertical and striae on the fault surface indicate a left-lateral horizontal movement. Significant vertical slip occurred exclusively within the compressive step and is estimated to

250 m [25]. Elsewhere, the fault trace is defined by abnormal contact between geological units and/or by breccia. No data exist on the deep structure of the PFZ, but there is no argument for a major change with depth in the fault geometry and the slip direction. At depth, the PFZ presumably roots within the Triassic décollement level situated at depth between 750 m in the north and 3 km in the south [26]. Correlation between the geological units of both sides and 3-D palinspastic restorations [26] indicate that the PFZ was a left-lateral transcurrent fault (i.e. a large part of the strike-slip displacement caused offsets of fold axes since it postdated folding). The maximum total slip is around 10 km.

Natural and artificial outcrops are numerous and allow reconstruction of the stresses associated with the PFZ activity. Because erosion has been low in the Jura Mountains, the minor faults now visible in outcrops reflect the paleostress fields at shallow depth. Because horizontal block rotations in the Jura Mountains are less than 8° [27], the stress tensors reconstructed from minor faults reliably reflect the initial orientations of the principal stresses. Particular attention has been paid to collect fault-slip data of various attitudes in order to obtain a good accuracy on the stress orientation. All minor faults presented here formed during the PFZ activity, that is during the Jura Phase. A few minor faults (not presented here) developed during two moderate pre-orogenic events, a strike-slip fault one during the Eocene and an extensional one during the Oligocene [28]. Relative chronologies with regard to the Oligocene faults and fractures (N–S to NW–SE normal faults and tension gashes) were used to date the compressional structures; faults that predate the extensional structures belong to the Eocene event, whereas faults that postdate the extensional structures formed during the Late Miocene event. Eocene and Oligocene features are not discussed in this paper. We focus on the PFZ activity (and associated secondary faulting) that occurred during the Late Miocene.

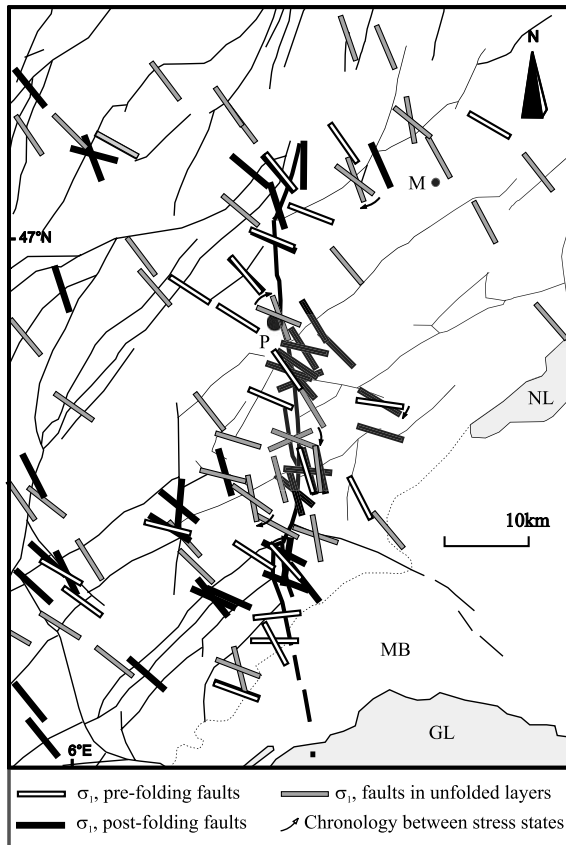


Fig. 11. Distribution of the Late Miocene compression around the PFZ inferred from inversion of minor faults. The PFZ is shown as a thick line. Calculated stress regimes are mainly of strike-slip type. When reverse faults are also present, the compression directions of the strike-slip and reverse regimes are similar. Order of superimposed stress states is inferred from relative chronology data between brittle structures (e.g. cross-cutting relationships between faults, superimpositions of striations on fault surfaces). The chronology between faulting and folding is indicated for folded sites (see text for explanation). Major faults are shown as thin lines. MB: Molasse Basin (limits in dashed lines); NL and GL: Neuchâtel and Geneva Lakes. P and M: cities of Pontarlier and Morteau.

3.2. Stresses around the PFZ

Inversion of 1500 minor faults at 58 stations

allowed reconstruction of the Late Miocene stress states near and away from the PFZ (Fig. 11). Most faults are right-lateral and left-lateral strike-slip faults. At some sites, reverse faults indicate a direction of maximum compression (σ_1) similar to that inferred from strike-slip faults. In such sites, the direction of compression is thus representative of both the strike-slip and reverse regimes. In this paper, we do not discuss such permutation between the principal axes σ_2 and σ_3 , but we focus on the orientation of the maximum compression, σ_1 . In most sites located far away from the PFZ, the fault population was produced by a homogeneous stress field corresponding to a NW–SE compression (Fig. 11). Because this direction is similar to that recognized in the neighboring poorly deformed areas of the Jura [21], faulting away from the PFZ has thus developed in response to the undisturbed far-field loading. In contrast, the stress pattern near the PFZ is heterogeneous. At some sites, the direction of compression differs substantially from the NW–SE far-field compression, implying clockwise and counterclockwise rotations (Fig. 11). At other places, minor faults collected in one station are mechanically incompatible, indicating that stresses have changed through time (Fig. 9). Homogeneous fault subsets were identified and analyzed separately. In such polyphase sites, the two calculated successive compressions make an angle ranging from 20° to 45° (Fig. 11).

Because the minor faults originated at moderate depths, the stresses responsible for their formation likely followed Anderson's model [29], according to which one principal stress is vertical and corresponds to the lithostatic pressure. In the present-day configuration, 21% of the calculated stress states do not fit Anderson's model, but exhibit two principal stresses lying within the bedding plane (the third one being thus perpendicular to the bedding plane). Such a geometrical relationship means that before bed tilting these two principal stresses were horizontal (the third one thus being vertical). In other words, stresses are in agreement with Anderson's model considering that the corresponding faults predated folding. The original stress attitude is restored by back-tilting (rotation around the local bed strike

of the amount of tilting) the corresponding faults. Systematic examination of the agreement of the calculated stress states with Anderson's model and of the misfits between faults and the calculated stress state allowed us to distinguish pre-folding and post-folding stress states. Considering the uncertainties on the calculated stress orientations and the possible slight deviation of one principal stress relative to the vertical, a reliable dating of faulting relative to folding requires at least an amount of tilt of the beds of 20°. Figs. 12 and 13 show the early (pre-folding) and the late (post-folding) stress fields around the PFZ which will now be considered separately.

3.3. Kinematics of the PFZ

Both the early and late stress fields (Figs. 12 and 13) are heterogeneous, exhibiting deflections as large as 45° with respect to the NW–SE far-field compression. Because stress deflections are located near the fault zone, they are very likely related to the PFZ activity. Comparison of the two successive stress fields reveals that stress deviations do not occur at the same localities (Fig. 11). This suggests that activity has migrated along the PFZ, i.e. the active strands of the fault zone were different through time.

For the late stress field (Fig. 12), most localities along the PFZ exhibit stress deflections. This suggests that, during this late stage, the whole PFZ may have undergone slip. In order to test this hypothesis, we have built a model simulating slip along the whole PFZ (Fig. 12). This model includes the two master faults, as well as the short linking segment. The applied far-field stresses correspond to a strike-slip regime with σ_1 trending N130°E, in accordance with the homogeneous orientation of the Late Miocene compressional stress in the poorly deformed areas of the Jura Mountains [21]. Magnitudes of the far-field principal stresses are derived from the differential stress values inferred from calcite twins analysis in the neighboring Burgundy platform [30] for a mean fault depth of 1 km, i.e. the middle of the cover. Elastic properties of the host rock were chosen according to static and dynamic estimations in Jura Mountains rocks ([31,32], Mannia,

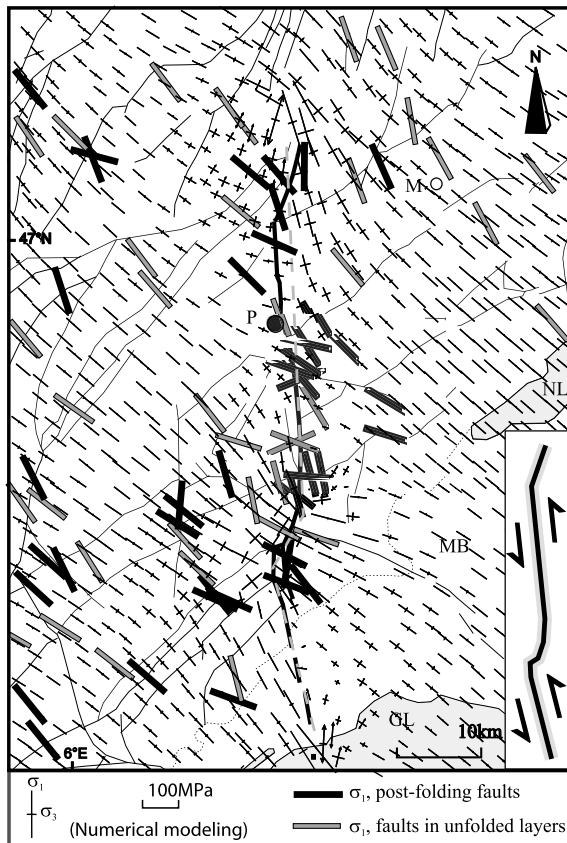


Fig. 12. Late stress field around the PFZ and theoretical static stress field following slip of the whole PFZ. The local stress states define the late stress field around the PFZ after folding and thrusting of the cover. The theoretical static stress field is obtained from a numerical modeling simulating slip on all segments of the PFZ. The PFZ has been divided into three segments (dashed gray line) with normal and shear stiffness equal to 200 MPa and coefficient of friction equal to 0.01. The applied far-field stress regime is a strike-slip regime with σ_1 trending NW–SE and corresponds to the far-field Mio–Pliocene stresses recognized in poorly tectonized areas of the Jura Mountains [21]. $\sigma_{2\infty}$ corresponds to the lithostatic load at 1 km depth and equals 25 MPa. Adopting the mean values for the differential stress $(\sigma_1 - \sigma_3)_\infty$ and $(\sigma_1 - \sigma_2)_\infty$ of 45 MPa and 20 MPa inferred from calcite twins analysis [30] gives magnitudes of the principal stresses $\sigma_{1\infty}$, $\sigma_{2\infty}$ and $\sigma_{3\infty}$ of 50 MPa, 25 MPa and 5 MPa. Young's modulus (E) and Poisson's ratio (ν) of the host rock equal 55 GPa and 0.29 according to static and dynamic elastic parameter estimates for various rocks of the Jura Mountains [31,32], and Mannia, personal communication). The stress deflection inferred from fault inversion fits those calculated by the numerical modeling and thus reflects a slip event along the whole PFZ (inset). Same symbols as in Fig. 11.

personal communication). The computed stress field fits well the late stress field inferred from minor fault analysis (Fig. 12). In the two compressional quadrants near the tips of each master fault, the compression is rotated in a clockwise sense, while it is rotated in counterclockwise sense in the two extensional quadrants and near the compressive step. Away from the PFZ, the compression regularly trends NW–SE. The close agreement between the calculated and actual stress fields leads us to conclude that the stress deflections inferred from the analysis of the late secondary faults reflects a slip event along the whole PFZ that occurred after folding of the cover. The numerical simulation of the stress deflections associated with this late fault activity requires a low friction on the active fault strand (Fig. 12). This suggests that during this period the PFZ behaved as a weak fault.

Because the early stress field took place before folding, we have restored the positions of measurement sites as well as the stress orientations before displacement and folding of the cover using the map restoration of Philippe et al. [26] based on serial balanced cross-sections. Fig. 13 shows the corresponding stress pattern. Near the northern master fault, the compression trends regularly NW–SE. This means that these parts of the PFZ were inactive at that time. On the other hand, the maximum compression trajectories are deflected close to the southern segment of the PFZ. These stress deviations resemble the theoretical stress rotations near the northern tip of a left-lateral fault (Fig. 4). The length of the active fault strand is unknown because the southern tip region is not documented, but the extent was at least 20 km long considering the area showing stress rotations (Fig. 13). The northern tip corresponded to that of the southern Pontarlier fault segment, just behind the present-day compressive step. The stress distribution of the early stress field thus reflects slip along the southern PFZ segment that occurred before folding and thrusting of the cover. Activity of the PFZ was thus first localized before folding along its southern branch (Fig. 13) and then migrated northward, involving the whole PFZ (Fig. 12). This is in agreement with the in-sequence Jura belt development [26].

4. Discussion

4.1. Stress sources

Slip events along fault systems that predated those recorded by historical and instrumental means may be inferred from the analysis of secondary faults. Our approach consists of comparing the stress fields reconstructed from inversions of numerous secondary faults collected in outcrops close and far from the fault zone with the SFS of a slip event on a fault (Figs. 3 and 7). The principle underlying this method is that stress deflections close to the fault are exclusively related to fault activity. Other sources of stress perturbations exist in the upper crust. We distinguish small-scale sources that modify stress orientation in limited areas and large-scale sources that affect stress orientation over large areas. An example of large-scale sources is the thrust pile of an orogenic system that indents the foreland, the compressive stress trajectories displaying a fan shape (e.g. [33]). Such large-scale sources do not prevent recognition of the fault-slip-related stress deflections because they induce stress deflections along the fault zone smooth and negligible with respect to the abrupt local changes in the stress direction induced by slip on the fault. Because the variations in the near-field stresses are dominated by the slip contribution, faults with a neighboring large-scale source display a slip-related SFS that resembles that of isolated fault zones.

Even if rocks differ on both sides of a fault zone, the stress states after a slip event on a fault still exhibit the characteristic clockwise and counterclockwise rotations near fault tips that allow recognition of the active fault strand. If small-scale sources exist, the stress field inferred from minor fault analysis should be compared to that calculated with a fault-slip model including these additional sources. This is especially the case where ‘passive sources’, i.e. sources that generate permanent stress perturbations, like strong or weak lithological bodies, are present. The case of a weak fault core has been considered in this paper (Figs. 6 and 7). Note that even if this weak body results in a more complex stress field, the slip-related SFS is still decipherable (compare

Figs. 3 and 7). ‘Active sources’, i.e. sources that induce transient stress deflections related to the source activity, like rapid fluid migration or magma chamber deflations, deserve consideration if they act simultaneously with the fault slip.

4.2. Application to other faults

In this paper, we have focused on vertical linear strike-slip fault zones. With appropriate numerical models, an active fault strand with any geometry may be reconstituted through analysis of stress deflections. It is worth noting that relatively complex slip events, like those involving en échelon fault segments, can be detected from our simplified linear fault model. As illustrated with the PFZ (Fig. 12), the stress distribution that follows slip on segmented faults still exhibits the characteristic deflections in the compressive and extensive quadrants near each master fault, allowing direct recognition of the active fault strands. When the slip event involves faults with a more complex geometry, like faults at high angle to each other, a refinement of the model describing the SFS of the slip event is required for a rigorous analysis of stress deflections. Similarly, the SFS approach can be extended to reverse and normal fault zones through a 3-D modeling.

4.3. Application to earthquake rupture

Although their ages are not well constrained, the two main periods of fault activity along the Tertiary PFZ were likely separated by a time period of the order of several million years. Slip events that are closer in age, like slips during large earthquakes, should also alter the stress field in the surrounding crust. For each slip event, the post-earthquake stress field should exhibit a SFS similar to that simulated in our theoretical numerical model (Figs. 3 and 7). Because the direction of fault slips on nearby secondary faults will be controlled by this modified stress field, analysis of these secondary fault slips will have the potential to constrain the location of the active fault strand for this slip event. This approach is especially useful for ruptures older than those recorded by instrumental means. Recognition of

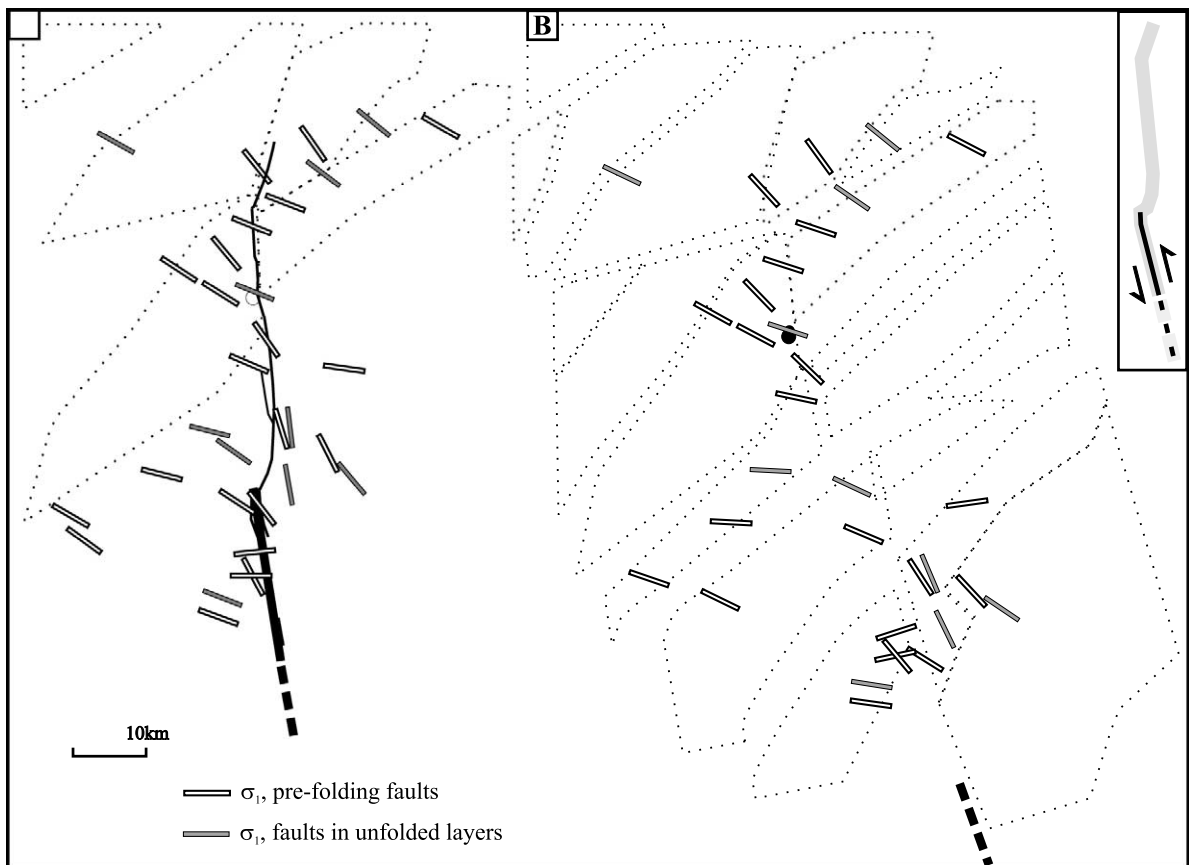


Fig. 13. Early stress field around the PFZ. The stress states associated with the early stress field (before folding and thrusting) are shown in their present-day position (A) and in their palinspastic positions (B) before folding and thrusting of the cover using the map restoration of Philippe et al. [26]. Blocks used for the cover restoration (dotted lines) are rigid. The shortening inferred from serial balanced cross-sections is shown as white space in front of each block. The early stress field is almost homogeneous in the northern part of the PFZ, but exhibits stress deflections close to the southern fault similar to those near one tip of an active fault strand (see Fig. 3). They thus reflect a slip event involving the southern fault of the PFZ (thick line) whose southern extension is unknown (inset).

such ancient ruptures through secondary fault analysis requires that the post-earthquake stress rotations are greater than the 10° accuracy on the stress orientations derived from secondary faults. This was the case for the Landers earthquake according to Hardebeck and Hauksson [34]. The calculated 20° stress rotation after the Landers earthquake is probably a minimum estimate because the stress tensor calculation was performed by inversion on focal mechanisms in large volumes that may contain stress discontinuities according to our model (Figs. 3 and 7). The SFS method could thus be relevant for recogni-

tion of ancient ruptures in fault zones producing earthquakes with significant stress drop relative to the background deviatoric stress in order to induce significant stress rotations. Recognition of successive ruptures along a fault zone requires that the slip event-related perturbations are relaxed over the seismic cycle, so that the stress field returns to the pre-event, far-field level before each individual slip event. This assumption seems reasonable considering that many small earthquakes occur between two large events, but further geological observations of the SFS adjacent to fault zones will make it possible to extend our knowl-

edge of the stress field beyond a single seismic cycle.

Concerning the PFZ, our analysis does not allow us to determine whether the two periods of fault activity revealed by the SFS method correspond to instantaneous ruptures (earthquakes) or steady-state slips. In any case, the fault activity during these two periods is correlated with the fault zone segmentation. During the pre-folding period, the fault activity occurred on the southern Pontarlier fault (Fig. 12) and involved the two master faults during the post-folding period (Fig. 13). Each period likely included a number of individual slip events, so that our analysis reveals a succession of dominating active segments rather than a succession of individual slips. However, for each period, the stress field has a unique SFS suggesting that these individual slips occurred on the same fault strand. This is in agreement with a characteristic behavior of the PFZ.

5. Conclusions

A systematic numerical modeling led us to define the SFS of a slip event on a strike-slip fault zone. The static stress field that follows a slip event has a typical pattern whatever the fault strike, fault properties and far-field stresses; it exhibits characteristic stress deflections in the compressive and extensive quadrants near the fault tips that indicate the position of the active fault strand. The subsequent secondary faults with millimetric to decimetric slip developing in the host rock differ according to the deflections of the stress state. Past slip events can thus be inferred by comparing the past stress fields inferred from inversion of minor faults collected in outcrops with the slip event SFS. Application of this method to the Tertiary 70-km-long PFZ allowed identification of two successive slip events and indicated that the fault activity has migrated northward, in agreement with the in-sequence belt development. Our results also suggest that the PFZ was a weak fault and followed a characteristic behavior. Both ancient and active fault zones can be investigated through this approach. Where proper markers are lacking, the SFS method of-

fers the opportunity to reconstruct the past slip history of fault zones with accurate location of ruptured fault strands.

Acknowledgements

We are grateful for the thoughtful review by Matthew d'Alessio and useful remarks of Vincent Courtillot. We thank Richard Schultz who greatly enhanced the quality of the English text. This work was supported by the Université Pierre et Marie Curie and the CNRS. [VC]

References

- [1] R.E. Wallace, Grouping and migration of surface faulting and variations on slip rates on faults in the great basin province, *Bull. Seismol. Soc. Am.* 77 (1987) 868–876.
- [2] D.J.A. Andrews, A stochastic fault model, *J. Geophys. Res.* 85 (1980) 3867–3877.
- [3] D.A. Von Seggern, A random stress model for seismicity statistics and earthquake prediction, *Geophys. Res. Lett.* 7 (1980) 637–640.
- [4] S.G. Wesnousky, The Gutenberg–Richter or characteristic earthquake distribution, which is it?, *Bull. Seismol. Soc. Am.* 84 (1994) 1940–1959.
- [5] K. Sieh, The repetition of large-earthquake ruptures, in: *Earthquake Prediction: The Scientific Challenge*, Natl. Acad. Sci. Proc., 1996, pp. 3764–3771.
- [6] Y. Kagan, Statistics of characteristic earthquakes, *Bull. Seismol. Soc. Am.* 83 (1993) 7–24.
- [7] G.C.P. King, R.S. Stein, J. Lin, Static stress and the triggering of earthquakes, *Bull. Seismol. Soc. Am.* 84 (1994) 935–953.
- [8] C. Maronne, Laboratory-derived friction laws and their application to seismic faulting, *Annu. Rev. Earth Planet. Sci.* 26 (1998) 643–696.
- [9] A. Gudmundsson, C. Homberg, Evolution of stress fields and faulting in seismic zones, *Pure Appl. Geophys.* 154 (1999) 257–280.
- [10] Y. Okada, Internal deformation due to shear and tensile faults in a half-space, *Bull. Seismol. Soc. Am.* 82 (1992) 1018–1040.
- [11] P. Segall, D.D. Pollard, Mechanics of discontinuous faults, *J. Geophys. Res.* 85 (1980) 4337–4350.
- [12] S. Toda, R.S. Stein, P.A. Reasenber, J.H. Dieterich, A. Yoshida, Stress transferred by the 1995 $M_w = 6.9$ Kobe, Japan, shock: effect on aftershocks and future earthquake probabilities, *J. Geophys. Res.* 103 (1998) 24543–24565.
- [13] O. Lacombe, J. Angelier, D. Byrne, J.M. Dupin, Eocene–Oligocene tectonics and kinematics of the Rhine-Saône

- continental transform zone (Eastern France), *Tectonics* 12 (1993) 874–888.
- [14] C. Homberg, J.C. Hu, J. Angelier, F. Bergerat, O. Lacombe, Characterization of stress perturbation near major fault zones: insights from 2-D distinct-element numerical modelling and field studies (Jura mountains), *J. Struct. Geol.* 19 (1997) 703–718.
- [15] F. Bergerat, J. Angelier, C. Homberg, Tectonic analysis of the Husavik-Flatey Fault (northern Iceland) and mechanisms of an oceanic transform zone, the Tjörnes Fracture Zone, *Tectonics* 19 (2000) 1161–1177.
- [16] G.C. King, Role of fault bends in the initiation and termination of earthquake rupture, *Science* 228 (1985) 984–987.
- [17] P.A. Cundall, UDEC, a generalised distinct element program for modelling jointed rock, U.S. Army Eur. Res. Office and Defence Nucl. Agency Contract Rep. DAJA (1980) 37-39-C-0548.
- [18] J.D. Byerlee, Friction of rocks, *Pure Appl. Geophys.* 116 (1978) 615–626.
- [19] J. Angelier, Inversion of field data in fault tectonics to obtain the regional stress. III: A new rapid direct inversion method by analytical means, *Geophys. J. Int.* 103 (1990) 363–376.
- [20] J. Angelier, F. Bergerat, H.T. Chu, Plate collision and paleostress trajectories in a fold-and thrust belt: the Foot-hills of Taiwan, *Tectonophysics* 125 (1986) 161–178.
- [21] C. Homberg, O. Lacombe, J. Angelier, F. Bergerat, New constraints for indentation mechanisms in arcuate belts from the Jura Mountains case (France), *Geology* 7 (1999) 827–830.
- [22] F. Bergerat, Stress fields in the European platform at the time of Africa-Eurasia collision, *Tectonics* 6 (1987) 99–132.
- [23] M. Burkhard, Aspects of the large-scale Miocene deformation in the most external part of the Swiss Alps (Sub-alpine Molasse to Jura fold belt), *Eclogae Geol. Helv.* 83 (1990) 779–780.
- [24] H.P. Laubscher, Jura kinematics and the Molasse basin, *Eclogae Geol. Helv.* 85 (1992) 653–675.
- [25] D. Aubert, Le décrochement de Pontarlier et l'orogénèse jurassienne, *Mém. Soc. Vaud. Sci. Nat.* 12 (1959) 93–152.
- [26] Y. Philippe, B. Colletta, E. Deville, A. Mascle, The Jura fold-and-thrust belt: a kinematic model based on map-balancing, in: P.A. Ziegler, F. Horvath (Eds.), *Structure and Prospects of Alpine Basins and Forelands, Peri-Tethys Memoir 2*, Muséum d'Histoire Naturelle, Paris, 1996, pp. 235–2611.
- [27] A. Gehring, P. Keller, F. Heller, Paleomagnetism and tectonics of the Jura arcuate mountain belt in France and Switzerland, *Tectonophysics* 186 (1991) 269–278.
- [28] C. Homberg, F. Bergerat, Y. Philippe, O. Lacombe, J. Angelier, Structural inheritance and cenozoic stress fields in the Jura fold-and-thrust belt (France), *Tectonophysics* 327 (2002) 137–158.
- [29] E.M. Anderson, *The Dynamics of Faulting*, Oliver and Boyd, Edinburgh, 1948, 206 pp.
- [30] O. Lacombe, P. Laurent, Determination of principal stress magnitudes using calcite twins and rock mechanics data, *Tectonophysics* 202 (1992) 83–93.
- [31] R. Riffaut, Catalogue des caractéristiques géologiques et mécaniques de quelques roches françaises, Intern. Rep. Lab., Central Ponts et Chaussées, DGRSR (1969) 150 p.
- [32] P. Broquet, J. Mania, N. Rampnoux, Anisotropie acoustique et sismique de calcaires fissurés aquifères, *Bull. Soc. Géol. Fr.* 164 (1993) 553–563.
- [33] P. Huchon, E. Barrier, J.C. de Bremaecker, J. Angelier, Collision and stress trajectories in Taiwan: a finite element model, *Tectonophysics* 125 (1986) 179–191.
- [34] J.L. Hardebeck, E. Hauksson, Crustal stress field in southern California and its implication for fault mechanics, *J. Geophys. Res.* 106 (2002) 21859–21882.